

# Strain-controlled high harmonic generation with Dirac fermions in silicene

Rui Qin<sup>\*,†,‡</sup> and Zi-Yu Chen<sup>\*,†,‡</sup>

<sup>†</sup>*National Key Laboratory of Shock Wave and Detonation Physics, Institute of Fluid Physics, China Academy of Engineering Physics, Mianyang 621999, China*

<sup>‡</sup>*these authors contributed equally to this work.*

E-mail: qinrui.phy@outlook.com; ziyuch@caep.ac.cn

## Abstract

Two-dimensional (2D) materials with zero band gap exhibit remarkable electronic properties with wide tunability. High harmonic generation (HHG) in such materials offers unique platforms to develop novel optoelectronic devices at nanoscale, as well as to investigate strong-field and ultrafast nonlinear behaviour of massless Dirac fermions. However, control of HHG by modulating electronic structure of materials remains largely unexplored to date. Here we report controllable HHG by tuning the electronic structures via mechanical engineering. Using an *ab initio* approach based on time-dependent density-functional theory (TDDFT), we show that the HHG process is sensitive to the modulation of band structures of monolayer silicene. Under small biaxial and uniaxial strains, large anisotropy and anharmonicity can be induced in the band structure while preserving the Dirac cones, which can lead to significantly enhanced harmonic intensity and broadened spectral width. With a small uniaxial strain of only 6%, the enhancement of HHG intensity can reach an order of magnitude. With the additional advantage of silicene in compatibility and integration into the current silicon-based electronic industry, this study may open a new avenue to develop efficient

solid-state optoelectronic nano-devices of extreme-ultraviolet and attosecond pulses, and provide a valuable tool to understand the strong-field and mechanically induced ultrafast nonlinear response of Dirac carriers in 2D materials.

## Keywords

high harmonic generation; 2D materials; mechanical engineering

## Introduction

The recent active investigations on high harmonic generation (HHG) from solid-state materials has opened up exciting opportunities in both fundamental physics and potential applications.<sup>1-5</sup> It provides an unique platform for the study of strong-field and ultrafast electron dynamics in the condensed phase.<sup>6</sup> HHG has been demonstrated as an attracting tool to explore the electronic structure of bulk crystals.<sup>7-11</sup> Experimental reports such as all-optical reconstruction of band structure of ZnO,<sup>12</sup> retrieving energy dispersion profile of the lowest conduction band of SiO<sub>2</sub>,<sup>13</sup> and measurement of the non-vanishing Berry curvature in symmetry-broken  $\alpha$ -quartz,<sup>14</sup> etc., mark some of the impressive advancement. HHG in solids also offers a promising approach for the development of novel compact coherent light sources in the extreme ultraviolet (XUV) and soft x-ray spectral region,<sup>15</sup> as well as for multi-petahertz-frequency optoelectronic<sup>16</sup> and attosecond photonics.<sup>17</sup> High harmonics and/or attosecond pulses can be shaped in terms of polarization and carrier-envelop phase,<sup>18,19</sup> and enhanced by means of tailored semiconductors<sup>20</sup> and metallic nanostructures.<sup>21</sup>

In addition to bulk solids, two-dimensional (2D) materials have also attracted considerable attention for HHG which exhibit distinctive electronic properties. Monolayer *h*-BN driven by out-of-plane laser fields has been calculated to exhibit atomic-like HHG while with a more favorable wavelength scaling.<sup>22</sup> Driven by in-plane fields, enhanced HHG efficiency from isolated monolayer MoS<sub>2</sub> compared to the bulk has been measured.<sup>23</sup> Besides, there are

a few theoretical and experimental investigations of HHG from 2D materials with massless Dirac fermions (MDF), though so far limited to graphene.<sup>24–30</sup> The study of nonperturbative HHG from such zero-gap 2D materials offers new possibilities to access strong-field and ultrafast nonlinear dynamics of MDF.<sup>31</sup>

Silicene, as the 2D form of silicon and the silicon analogue of graphene, also exhibits exceptional electronic properties such as MDF behavior, linear energy dispersion, and a high Fermi velocity. In addition, as silicon being the element of IV family close to carbon, silicene has apparent advantage over graphene in compatibility and integration into the current silicon-based electronic industry. Thus, HHG from silicene, which has not been studied before, is highly relevant not only for investigating the remarkable properties of massless Dirac quasiparticles, but also for developing future integrated all-optical solid-state devices at nanoscale.

Being amenable to extensive nanoengineering technologies, the electronic properties of 2D materials can display very rich and complex phenomenons and wide tunability, which can have significant influence on HHG process. Realization of controllable HHG in 2D Dirac materials by tuning the electronic properties is important for novel device applications and to infer ultrafast dynamics of MDF. To date, however, HHG control by tuning the electronic properties has remained largely unexplored. Moreover, the reported theoretical investigations of HHG from Dirac materials are all based on simplified models without properly considering the full electronic and real crystal structures.

In this work, we report, to our knowledge, the first controllable HHG by tuning the electronic structures via mechanical engineering. HHG in silicene monolayer under different strain profiles are investigated using an *ab initio* approach based on the framework of time-dependent density-functional theory (TDDFT).<sup>32–34</sup> We use the methods established recently by Tancogne-Dejean *et al.*<sup>11,18,22</sup> The first-principles simulation results show that the electronic band structures of silicene and the related HHG are sensitive to strains. Strain engineering can be a promising strategy for controlling HHG and studying MDF dynamics

in 2D materials.

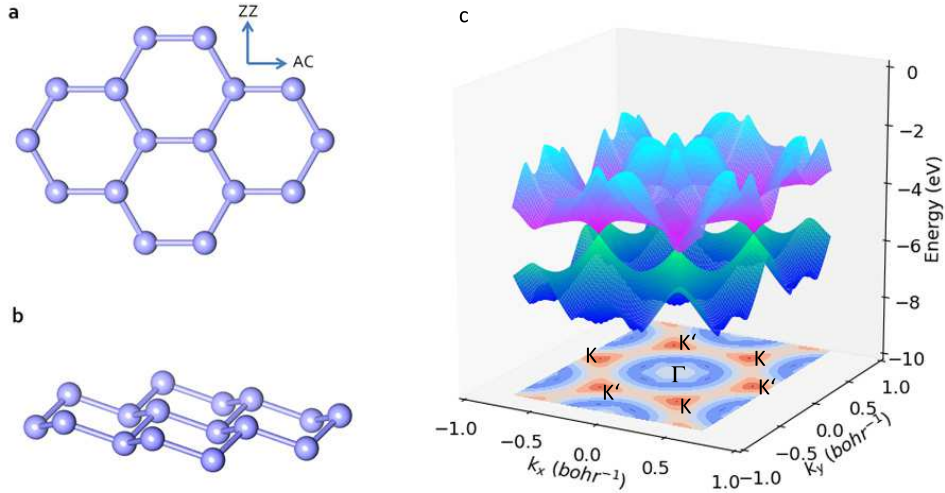


Figure 1: (a) Top and (b) side views of the crystal structure of the silicene monolayer. The definition of the armchair (AC) and zigzag (ZZ) directions are shown in panel a. (c) Energy dispersion surface of the highest valence band and lowest conduction band of silicene without strain. Projection of the highest valence band with high symmetry points marked is also shown.

## Results

With a 2D honeycomb lattice structure like graphene, silicene is predicted to favor a low-buckled structure<sup>35</sup> (Fig. 1a, b). In this study, the geometric structures of silicene are obtained by using the Octopus package. The calculated lattice constant of the hexagonal lattice, Si-Si bond length, and the buckling distance for silicene without strain are 3.81, 2.24, and 0.42 Å, respectively, which are in good agreement with previous calculations.<sup>36,37</sup> We also calculate the electronic structure of silicene without strain. The energy dispersion surface clearly shows the Dirac cones at the Brillouin zone (BZ) boundary at the Fermi level (Fig. 1c), which induces the massless Dirac fermion behavior near the Fermi level like graphene. Uniform biaxial and uniaxial strain are applied to silicene to investigate the strain effect on HHG. Two special directions of silicene, the armchair (AC) and zigzag (ZZ) directions are marked in Fig. 1a. In our calculations, strain  $\varepsilon$  is defined as  $\varepsilon = (a - a_0)/a_0$ , where  $a$  and

$a_0$  are the lattice constants with and without strain, respectively. Lattices under the biaxial and uniaxial strains are changed following our previous studies.<sup>36,37</sup> The atomic structures are relaxed for the new lattice constant after each time when we change the lattice constants.

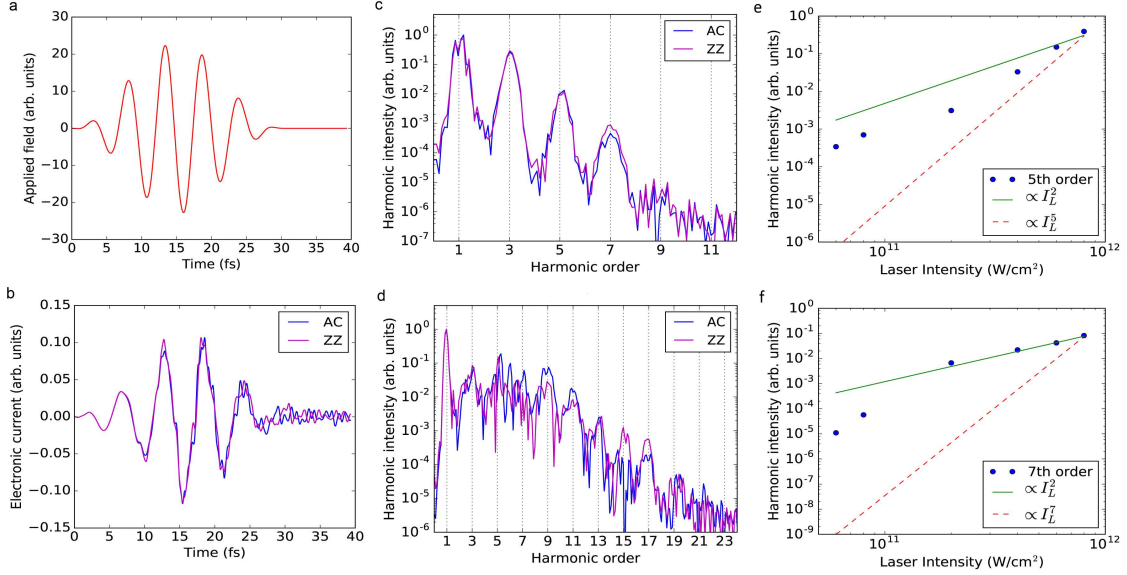


Figure 2: (a) The applied vector potential and (b) induced electronic currents with a laser wavelength of 1600 nm, pulse duration of 15 fs, and intensity of  $8 \times 10^{11}$  W/cm<sup>2</sup>. Computed HHG spectra from silicene without strain with laser intensity of (c)  $8 \times 10^{10}$  W/cm<sup>2</sup> and (d)  $8 \times 10^{11}$  W/cm<sup>2</sup>. Intensity scaling for the (e) 5th and (f) 7th harmonics, demonstrating the harmonic generation in this study is in the nonperturbative regime. The blue dots are the simulation data, while the solid green and dashed red lines are for theoretical fitting.

Figures 2a-b show the typical profiles of the applied vector potential and induced electronic currents, respectively, where the laser wavelength is 1600 nm and pulse full-width at half-maximum (FWHM) duration is 15 fs. The current waveforms are distorted which contain harmonic components of the driving laser pulse. Figures 1c shows the HHG spectra from a monolayer silicene without strain with a driving laser intensity of  $8 \times 10^{10}$  W/cm<sup>2</sup>. Only odd harmonic orders are present, reflecting the centrosymmetric nature of the crystal lattice. Up to the 7th harmonic order are obtained. It is worthy to note that the experimentally measured HHG from monolayer graphene is up to the 5th order<sup>30</sup> with a driving intensity of  $5.7 \times 10^{10}$  W/cm<sup>2</sup> and up to the ninth order<sup>29</sup> with a driving intensity of  $8 \times 10^{11}$  W/cm<sup>2</sup>. Considering the similarity of electronic structures between silicene and graphene,

our simulation results are in good agreement with the experimental observations, showing the reliability of our simulations. When the laser intensity is increased to  $8 \times 10^{11}$  W/cm<sup>2</sup>, higher-order harmonics are generated up to the 19th order, as shown in Fig. 2d.

Previous studies state that HHG is isotropic in graphene due to rotational symmetry in the band structure of the Dirac cone.<sup>29,30</sup> Here we consider laser polarization orienting along two specific directions, i.e., the AC and ZZ directions. Simulation results show evidently different HHG spectra between the two directions, which are pronounced for higher-order harmonics and higher laser intensity (see Figs. 2c-d). Therefore, even 2D materials with symmetric Dirac cone exhibit anisotropic emission of high harmonics. On the other hand, the anisotropic HHG spectra reflect the symmetries of the energy dispersion in the BZ. We note that the band structure is isotropic only in the vicinity of the Dirac points. It is significantly anisotropic away from the Dirac points (see Fig. 1c). Further increasing anisotropy of the band structure by strain engineering is thus expected to result in enhanced anisotropic HHG emission for different laser polarization. More importantly, modulated band structure by strain engineering should also lead to significant change in the HHG spectra compared to the case where no strain is applied.

Figures 2e-f show the intensity of 5th and 7th harmonics as a function of the pump laser intensity  $I_L$ , respectively. Both show a characteristic power law scaling of  $\propto I_L^2$ , demonstrating the HHG in this study is in the nonperturbative regime. Otherwise, they would scale as  $\propto I_L^5$  for the 5th-harmonic and  $\propto I_L^7$  for the 7th-harmonic if it was in the perturbative limit.

The computed HHG spectra of silicene controlled by strain engineering are presented in Fig. 3. We first investigate the case of a small laser intensity, i.e.,  $I_L = 8 \times 10^{10}$  W/cm<sup>2</sup> at wavelength of 1600 nm and duration of 15 fs (see Figs. 3a-b). For the case of uniform biaxial strain applied, the silicene structure maintains the hexagonal symmetry while with an elongate lattice constant. Comparing to the no strain case, although the strain is as small as 6%, the intensity of the 5th harmonics is greatly enhanced, which is more than 6 and 4 times stronger for the AC and ZZ laser polarization configurations, respectively (see Figs.

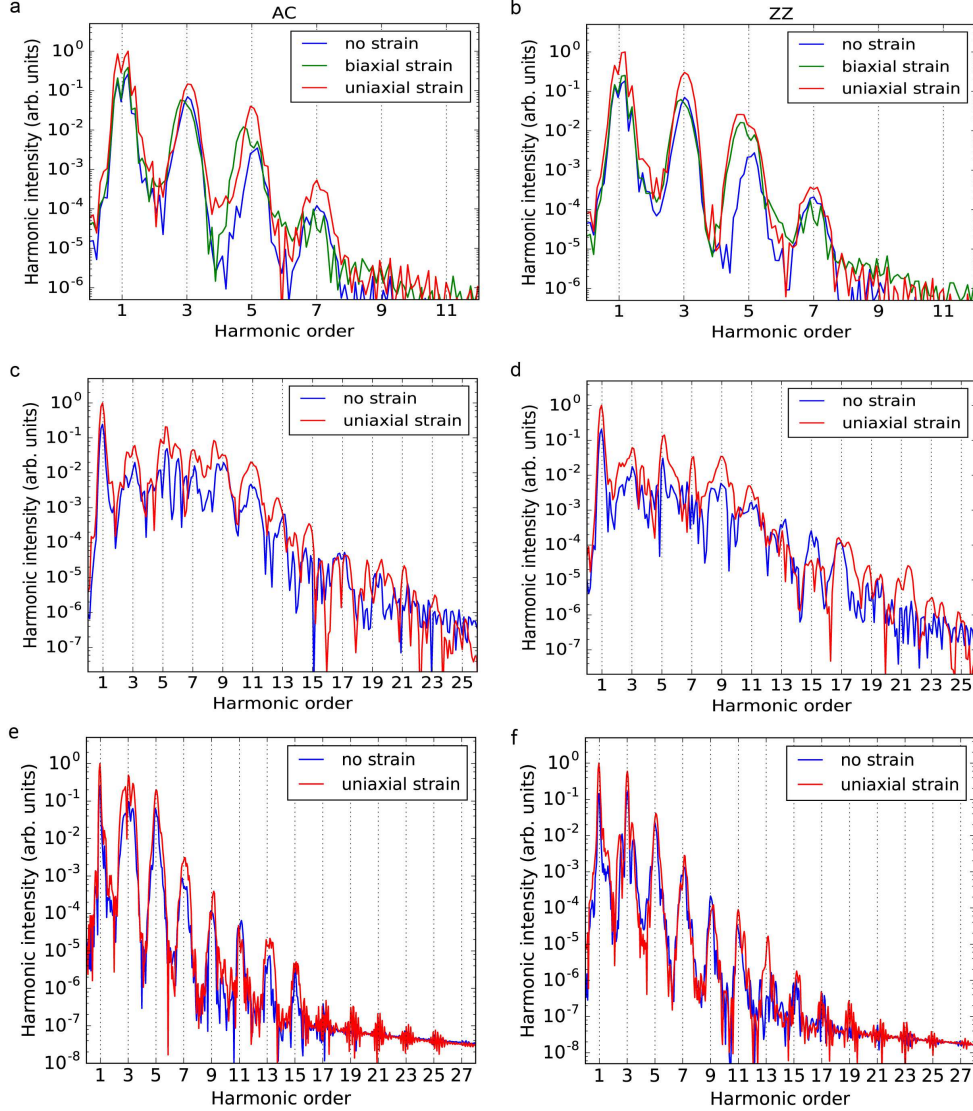


Figure 3: HHG spectra from silicene under different strain profiles and laser parameters. (a)-(b) are for laser wavelength of 1600 nm and intensity of  $8 \times 10^{10}$  W/cm<sup>2</sup>. (c)-(d) are for laser wavelength of 1600 nm and intensity of  $8 \times 10^{11}$  W/cm<sup>2</sup>. (e)-(f) are for laser wavelength of 800 nm and intensity of  $2.5 \times 10^{12}$  W/cm<sup>2</sup>. In all panels, laser pulse duration is 15 fs. Both biaxial and uniaxial strains are of six percent. (a), (c), and (e) correspond to the configurations of laser polarization orienting along the AC directions, while (b), (d), and (f) correspond to ZZ directions.

3a-b). Meanwhile, the intensity of other harmonic orders is nearly unchanged for both laser polarization configurations. In addition to the intensity enhancement, the FWHM of the 5th harmonic peak increases by a factor of about 1.7 and 1.6 for the AC and ZZ laser polarization configurations, respectively.

For the case of applying uniaxial strain, the symmetry of silicene is broken, which is expected to bring new features to HHG. In this work, we only consider the effect of tensile strain along the ZZ direction for demonstration. Due to Poisson's effect, the lattice constant along the AC direction decreases when the lattice is stretched along the ZZ direction. Consequently, the geometric structure and BZ no longer maintain the regular hexagonal symmetry. For the HHG spectra under uniaxial strain of 6%, in contrast to the biaxial strain case under the same strain, not only the 5th harmonic order, but also the other harmonic orders are all significantly enhanced in intensity. The enhancement for the 5th harmonics reaches an order of magnitude, which is approximately 12 and 10 times compared to the no strain case for the AC and ZZ laser configurations respectively, larger than that of the biaxial strain case (see Figs. 3a-b). Moreover, the spectral width exhibits a strong anisotropic modulation. The FWHM of the 5th harmonic peak is broadened by 1.4 times for the ZZ laser configuration, while nearly unchanged for the AC laser configuration.

Figures 3c-d show the HHG spectra for a higher laser intensity of  $I_L = 8 \times 10^{11} \text{ W/cm}^2$  at wavelength of 1600 nm and duration of 15 fs. Higher-order harmonics up to about 21st order are evident. For both configurations of laser polarization, HHG intensity for most of the harmonic orders is greatly enhanced by applying a 6% uniaxial strain. Besides, the enhancement by mechanical strain also works with a different driving wavelength. To illustrate this, we show the simulated spectra in Figs. 3e-f for a driving laser wavelength of 800 nm, pulse duration of 15 fs, and peak intensity of  $I_L = 2.5 \times 10^{12} \text{ W/cm}^2$ . Well defined high harmonic structures up to the 17th harmonic order can be clearly seen for the strain-free case (see Fig. 3f). By applying 6% uniaxial strains, HHG can be enhanced up to the 25th harmonic order extending to the XUV spectral region. These results demonstrate the



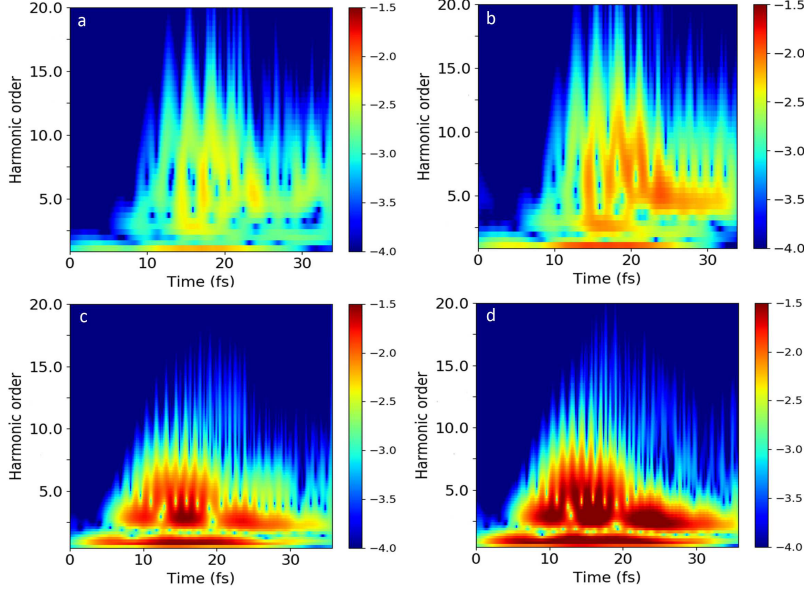


Figure 4: Harmonic order versus time for different laser and strain parameters: (a) 1600 nm,  $8 \times 10^{11}$  W/cm<sup>2</sup>, and no strain; (b) 1600 nm,  $8 \times 10^{11}$  W/cm<sup>2</sup>, and uniaxial strain; (c) 800 nm,  $2.5 \times 10^{12}$  W/cm<sup>2</sup>, and no strain; (d) 800 nm,  $2.5 \times 10^{12}$  W/cm<sup>2</sup>, and uniaxial strain. The laser polarization orients along the AC directions. Color shows the spectral intensity (arb. units) on a logarithmic scale.

potential for developing strain-controlled solid-state XUV source and attosecond photonics based on HHG in silicene under strain. Apart from these, all the spectra shown in Fig. 3 present odd orders only, reflecting the inversion symmetry protected under the biaxial and uniaxial strains.

Nonperturbative HHG in solids originates from two mechanisms, the intraband dynamics, i.e., laser-driven dynamic Bloch oscillation within the non-parabolic band, and interband contribution, i.e., direct electron-hole recombination between the conduction and valence bands. To gain insight into the radiation mechanism, we perform frequency-time analysis of the HHG. Figure 4 shows the spectrograms for different laser wavelength (1600 nm and 800 nm) and strain profiles (no strain and uniaxial strain), all of which reveal that the high harmonics are emitted as discrete bursts *in phase* at each peak of the laser field corresponding to maximum electron acceleration. The presence of the in-phase feature in the spectrograms instead of recombination trajectories shows strong evidence supporting that intraband con-

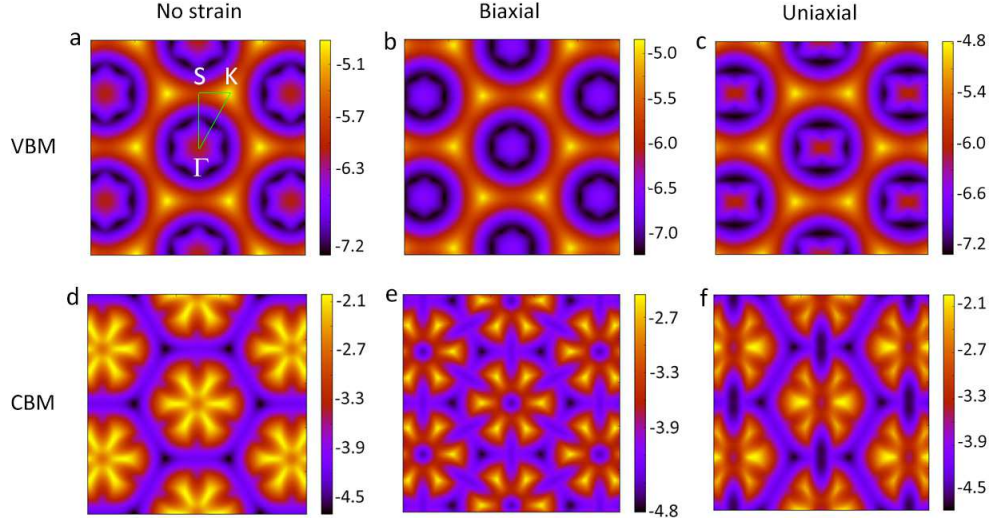


Figure 5: Contour plots of energy in reciprocal space of valence band maximum (VBM) ((a)-(c)) and conduction band minimum (CBM) ((d)-(f)) for three different strain profiles: no strain (first column), biaxial strain (second column), and uniaxial strain (third column). High symmetry points  $S$ ,  $K$ ,  $\Gamma$  in the first Brillouin zone are labeled in panel (a). The units of the color bars are eV.

tribution is the dominate mechanism<sup>38</sup> of the HHG we studied here. We note that previous model calculations also reveal that intraband contribution dominates the HHG in monolayer graphene.<sup>30</sup>

To understand the HHG enhancement under strains, we now study the electronic structure of silicene under different strain profiles, since the in-plane HHG is closely related to the band structure for 2D materials. First we explore the band structure over the whole BZ. In order to get a simple physical picture, we assume the HHG is mainly contributed by the highest valence band and lowest conduction band, which will be justified later. From Fig. 5a-c, we observe that the highest valence band does not change much under various strain profiles comparing to the lowest conduction band counterparts. Therefore we focus on the the lowest conduction band, especially the states near the Fermi level due to their large population of carriers. Without the presence of strain, the states with low energies all locate at the vicinity of the six K points (i.e., the Dirac cones). The area in which Dirac cones keep the rotational symmetry is also the largest among the three strain profiles (Fig. 5d-f).

For the biaxial strain case, although the BZ has the same symmetry as the no strain case, the area where the Dirac cones have rotational symmetry shrinks. Furthermore, besides the states around the Dirac cones, the states near the  $\Gamma$  point also locate closely above the Fermi level (Fig. 5e). For the uniaxial case, the BZ and band structure have a lower symmetry than those of the other two strain cases. Similar with the biaxial case, new states emerge closely above the Fermi level, but they locate near the S point and show high directivity in  $\Gamma$ -S direction (Fig. 5f). The lower the states in the conduction bands are, the more easily the free carriers can be excited by the laser field from the highest valence band to these lowered states, which can thus lead to enhanced HHG.

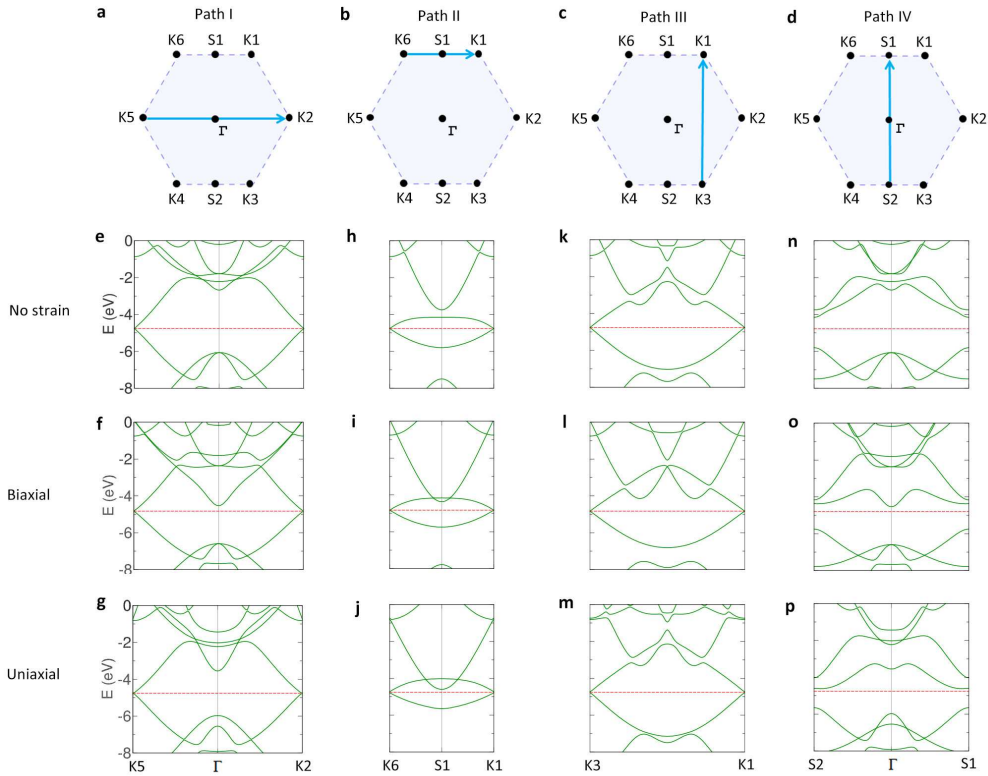


Figure 6: (a)-(d) Schematics of four representative paths in the Brillouin zone which correspond to the carrier dynamics. Band structures in the reciprocal space along (e)-(g) path I, (h)-(j) path II, (k)-(m) path III, and (n)-(p) path IV. The red dashed lines denote the Fermi level. The first two columns correspond to the configuration of laser polarization along the ZZ direction, and the last two columns correspond to the configuration of laser polarization along the AC direction.

We next analyse the paths in the BZ which correspond to the MDF dynamics in the

reciprocal space. For the sake of better illustration, we choose four representative paths where the states are close to the Fermi level, which are expected to have major contributions to the HHG process. Path I and II correspond to the ZZ laser polarization configuration (Fig. 6a-b), while path III and IV to the AC laser polarization configuration (Fig. 6c-d). Notice the direction in reciprocal and real space are opposite. Under the uniaxial strain, the Dirac points will shift parallel to the  $\Gamma$ -K2 direction.<sup>37</sup> However, they only shift very slightly in the considered small strain of 6% , thus we use the same paths for the uniaxial strain case as the other two strain cases for consistency. We first investigate MDF dynamics in the ZZ laser polarization configuration. Considering path I, when there is no strain, most of the states near the Fermi level are from the  $\pi^*$ -band. Besides, there is only a small overlap between the  $\pi^*$ - and  $\sigma^*$ -band near the  $\Gamma$  point in CBM (Fig. 6e). With the presence of strain, the overlap between the  $\pi^*$ - and  $\sigma^*$ -band becomes larger, and the states near the  $\Gamma$  points shift towards the Fermi level (Fig. 6f-g). The hybridization of  $\pi^*$ - and  $\sigma^*$ -band leads to a larger anharmonicity of CBM comparing to the no strain case, which may result in an enhanced contribution to the HHG via the intraband mechanism. In path II, we also observe this hybridization and enhanced anharmonicity of the CBM under strains (Fig. 6h-j). Thus both path I and II may have a contribution to the HHG enhancement in the ZZ laser polarization configurations. We also notice that in path I the states near the  $\Gamma$  points are closer to the Fermi level in the biaxial strain case (Fig. 6f) than those in the uniaxial strain case (Fig. 6g). However, the states in path II near the S1 point in the uniaxial strain case (Fig. 6j) are even closer to the Fermi level than those near the  $\Gamma$  point in the biaxial case in path I (Fig. 6f). Thus the CBM in the uniaxial strain case can have a higher carrier population, which may lead to the enhanced HHG intensity in the uniaxial strain case.

For the case of AC laser polarization configuration, from the band structures in path III, a small overlap between the  $\pi^*$ - and  $\sigma^*$ -band can be observed in the biaxial strain case (Fig. 6l) while these two bands remain untouched in the no strain (Fig. 6k) and uniaxial strain (Fig. 6m) cases. But for all strain cases most of the low-lying states still locate near

the Dirac points (Fig. 6k-m). Therefore this path contribute little to the change of HHG intensity under different strain profiles. In contrast, new states emerge close to the Fermi level under biaxial and uniaxial strains in path IV, which locate near the  $\Gamma$  and S points for the biaxial (Fig. 6o) and uniaxial (Fig. 6p) strains, respectively. The states in the uniaxial strain case (Fig. 6p) are even closer to the Fermi level than those in the biaxial case (Fig. 6o). Moreover, these states in the uniaxial strain case form a rather flat band near the S1 and S2 points (Fig. 6p) and thus induce a high density of states (DOS). The low-lying states near the S points with a high DOS can lead to a high carrier population. Consequently, this may result in a higher HHG intensity in the uniaxial strain case than in the other two strain cases.

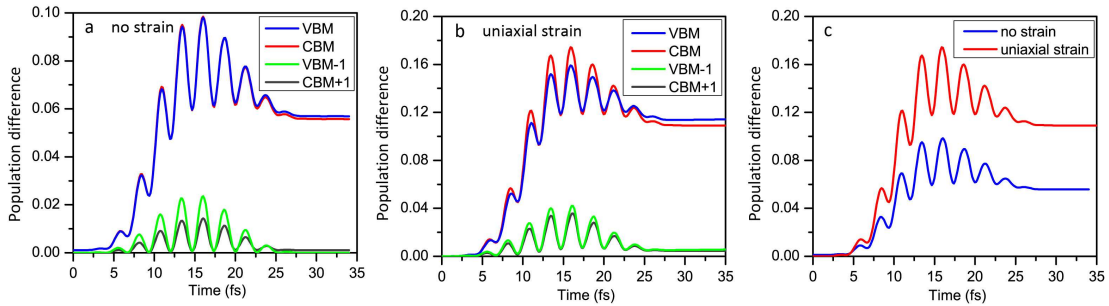


Figure 7: Temporal evolution of the population difference in various bands of silicene without strain (a) and under uniaxial strains (b). Here the population difference is defined as  $|N(t) - N(t=0)|$ , where  $N(t)$  and  $N(t=0)$  denote the electron population at time  $t$  and ground state ( $t=0$ ), and  $N(t=0)$  is 0 and 2 for conduction and valence band, respectively due to the spin-degeneracy. VBM, CBM, VBM-1, CBM+1 denote the valence band maximum, conduction band minimum, highest band below valence band maximum, and lowest band above conduction band maximum, respectively. (c) Comparison of population difference of CBM between silicene without strain and under uniaxial strain. The uniaxial strain is of six percent. Calculations in all panels correspond to the laser configuration of laser wavelength of 1600 nm, intensity of  $8 \times 10^{10}$  W/cm<sup>2</sup> and polarization of ZZ direction.

To further confirm the HHG enhancement can be attributed to increased number of excited electrons into conduction bands via strain-induced band structure modulation, we inspect the time evolution of population difference in various bands for the strain-free and uniaxial strain cases (see the Methods section for more technical details of population calculation). For both strain-free (Fig. 7a) and uniaxial strain (Fig. 7b) cases, the excited

electrons mainly come from the VBM. The valence bands below VBM contribute much less than VBM to carrier excitation. Also the electrons are mainly excited into CBM, and the conduction bands above CBM contains much less excited electrons. Thus it is a reasonable simplification to only consider the contributions of VBM and CBM to HHG in the silicene-like gapless materials, which is consistent with our previous analysis and previous two-band model-based calculations.<sup>30</sup> We also compare the population difference for different strain profiles. It is shown clearly in Fig. 7c that the electron population in CBM is much larger for the uniaxial strain case than that for the no strain case, which supports our band structure analysis that the strain-induced band structure modulation can change the number of excited carriers and thus the HHG in silicene. As mentioned above, intraband contribution dominates the HHG process in this study. However, we emphasise that HHG would be enhanced for both intraband and interband mechanisms if the population was increased. Other than the population increase, it should also be noted that the strain-induced band structure modulation also changes the curvature of the energy dispersion, which could be another possible contribution to the changed HHG intensity via the intraband mechanism.

The presence of strain changes the lattice structures of silicene, which changes the charge density. Moreover, strain also brings profound modulation to the electronic band structures, and consequently, the carrier density is further varied. These strain effects can lead to modification of the nonlinear refraction index of the material and thus phase changes of the light waves. Various nonlinear processes such as self-phase modulation and cross phase modulation may contribute to the spectral broadening shown in Fig. 3.

## Discussion

In summary, we have investigated tunable high-harmonic emission from a monolayer 2D material with Dirac fermions driven by in-plane electric fields using first-principles TDDFT calculations. We show that HHG in silicene can be actively controlled in terms of intensity

and spectral width by modulating the electronic properties of the 2D material via strain engineering. The HHG is sensitive to the electronic band structure modulations. The HHG intensity can be enhanced by an order of magnitude under a small uniaxial strain of only 6%. We identify the intraband contribution is the dominate HHG mechanism. The strain-induced band structure modulation can lead to increased number of excited electrons, which eventually results in enhanced HHG. Strain engineering of HHG should be applicable in other similar 2D materials with MDF, e.g., graphene. Many other approaches, such as using substrate, doping, and electrostatic gating, can also be introduced to tune the electronic properties and HHG in 2D materials. The study thus opens a new avenue to the development of compact solid-state optoelectronic nano-devices for tailored extreme-ultraviolet and attosecond pulses. It can also provide important insights for the investigation of strong-field and mechanically induced nonlinear response of Dirac carriers in 2D materials. By measuring the time evolution of HHG, it should be possible to obtain novel ultrafast dynamical information of the Dirac fermions. Besides, HHG offers a valuable tool to understand the strain effect on silicene monolayer, which is also of great importance for 2D material growth.

## Methods

Silicene structures are studied by using the semiperiodic supercell model. Silicene structures without strain and under biaxial strain are modelled by the hexagonal primitive cell containing two silicon atoms, while silicene structures under uniaxial strain are modelled by a rectangular supercell containing four silicon atoms. A vacuum of 30 Bohr, which includes 3 Bohr of absorbing regions on each side of the monolayer, is chosen to eliminate the interactions between adjacent silicene sheets and avoid the reflection error in the spectral region of interest. All calculations are performed by the Octopus package.<sup>39–41</sup> The ground state electronic structure properties and geometric structure relaxation are performed within the density functional theory (DFT) framework in the local density approximation (LDA).<sup>42</sup> Time

evolution of the wave functions and time-dependent electronic current are studied by propagating the Kohn-Sham equations in real time and real space<sup>43</sup> within the time-dependent DFT (TDDFT) framework in the adiabatic LDA (ALDA). The real-space spacing is 0.4 Bohr. A  $60 \times 60 \times 1$  Monkhorst-Pack  $k$ -point mesh for the BZ sampling is used for silicene without strain, and the sampling is scaled according to the size of the supercells. The fully relativistic Hartwigsen, Goedecker, and Hutter (HGH) pseudopotentials are used in all our calculations.

The laser is described in the velocity gauge. A sin-squared envelope and a carrier-envelope phase of  $\Phi = 0$  is used for the laser profile. The laser pulse duration is  $\tau=15$  fs. Laser wavelength of  $\lambda =1600$  nm (corresponding to a photon energy of 0.77 eV) and  $\lambda =800$  nm (corresponding to a photon energy of 1.55 eV) are considered. The peak laser intensity in vacuum is  $I_0 = 2.5 \times 10^{12}$  W/cm<sup>2</sup> for  $\lambda =800$  nm and in the range of  $I_0 = 8 \times 10^{10}$  W/cm<sup>2</sup> and  $I_0 = 8 \times 10^{11}$  W/cm<sup>2</sup> for  $\lambda =1600$  nm. The linearly polarized laser field is normally incident onto the silicene sample so that the driving electric field is in the plane of the monolayer.

The HHG spectrum was calculated from the total time-dependent electronic current  $\mathbf{j}(\mathbf{r}, t)$  as:

$$\text{HHG}(\omega) = \left| \text{FT} \left( \frac{\partial}{\partial t} \int \mathbf{j}(\mathbf{r}, t) d^3\mathbf{r} \right) \right|^2, \quad (1)$$

where FT denotes the Fourier transform.

Electron population of the band was calculated by the projection of the time-dependent Kohn-Sham states on the the ground-state Kohn-Sham states. As the  $n$ -th state evolves in time, it has some possibility to transit to other states and thus contain other ground-state components. The population that any occupied state has evolved into the  $m$ -th ground-state Kohn-Sham band is:

$$P(m, t) = \int_{\text{BZ}} \sum_n f_{n,k} |\langle \phi_{n,k}(t) | \phi_{m,k}(0) \rangle|^2 d\mathbf{k} \quad (2)$$

where  $\phi_{n,k}(t), \phi_{m,k}(0)$ ,  $f_{n,k}$ , BZ denote the time-dependent Kohn-Sham state at  $n$ -th band



at k-point  $k$ , the ground-state ( $t = 0$ ) Kohn-Sham state at  $m$ -th band at k-point  $k$ , and the occupation of Kohn-Sham state at  $n$ -th band at k-point  $k$ , integration over the whole Brillouin zone, respectively.

## References

1. Ghimire, S.; DiChiara, A. D.; Sistrunk, E.; Agostini, P.; DiMauro, L. F.; Reis, D. A. Observation of high-order harmonic generation in a bulk crystal. *Nature Physics* **2010**, *7*, 138–141.
2. Schubert, O.; Hohenleutner, M.; Langer, F.; Urbanek, B.; Lange, C.; Huttner, U.; Golde, D.; Meier, T.; Kira, M.; Koch, S. W. *et al.* Sub-cycle control of terahertz high-harmonic generation by dynamical Bloch oscillations. *Nature Photonics* **2014**, *8*, 119–123.
3. Vampa, G.; Hammond, T. J.; Thiré, N.; Schmidt, B. E.; Légaré, F.; McDonald, C. R.; Brabec, T.; Corkum, P. B. Linking high harmonics from gases and solids. *Nature* **2015**, *522*, 462–464.
4. Hohenleutner, M.; Langer, F.; Schubert, O.; Knorr, M.; Huttner, U.; Koch, S. W.; Kira, M.; Huber, R. Real-time observation of interfering crystal electrons in high-harmonic generation. *Nature* **2015**, *523*, 572–575.
5. Ndabashimiye, G.; Ghimire, S.; Wu, M.; Browne, D. A.; Schafer, K. J.; Gaarde, M. B.; Reis, D. A. Solid-state harmonics beyond the atomic limit. *Nature* **2016**, *534*, 520523.
6. Kruchinin, S. Y.; Krausz, F.; Yakovlev, V. S. Colloquium : Strong-field phenomena in periodic systems. *Reviews of Modern Physics* **2018**, *90*, 021002.
7. Vampa, G.; McDonald, C.; Orlando, G.; Klug, D.; Corkum, P.; Brabec, T. Theoretical

- Analysis of High-Harmonic Generation in Solids. *Physical Review Letters* **2014**, *113*, 073901.
8. Otake, T. High-harmonic generation in  $\alpha$ -quartz by electron-hole recombination. *Physical Review B* **2016**, *94*, 235152.
  9. Osika, E. N.; Chacón, A.; Ortmann, L.; Suárez, N.; Pérez-Hernández, J. A.; Szafran, B.; Ciappina, M. F.; Sols, F.; Landsman, A. S.; Lewenstein, M. Wannier-Bloch Approach to Localization in High-Harmonics Generation in Solids. *Physical Review X* **2017**, *7*, 021017.
  10. You, Y. S.; Reis, D.; Ghimire, S. Anisotropic high-harmonic generation in bulkcrystals. *Nature Physics* **2016**, *13*, 345349.
  11. Tancogne-Dejean, N.; Mcke, O. D.; Krtner, F. X.; Rubio, A. Impact of the Electronic Band Structure in High-Harmonic Generation Spectra of Solids. *Physical Review Letters* **2017**, *118*, 087403.
  12. Vampa, G.; Hammond, T.; Thiré, N.; Schmidt, B.; Légaré, F.; McDonald, C.; Brabec, T.; Klug, D.; Corkum, P. All-Optical Reconstruction of Crystal Band Structure. *Physical Review Letters* **2015**, *115*, 193603.
  13. Luu, T. T.; Garg, M.; Kruchinin, S. Y.; Moulet, A.; Hassan, M. T.; Goulielmakis, E. Extreme ultraviolet high-harmonic spectroscopy of solids. *Nature* **2015**, *521*, 498502.
  14. Luu, T. T.; Wrner, H. J. Measurement of the Berry curvature of solids using high-harmonic spectroscopy. *Nature Communications* **2018**, *9*, 916.
  15. Garg, M.; Kim, H. Y.; Goulielmakis, E. Ultimate waveform reproducibility of extreme-ultraviolet pulses by high-harmonic generation in quartz. *Nature Photonics* **2018**, *12*, 291296.

16. Garg, M.; Zhan, M.; Luu, T. T.; Lakhotia, H.; Klostermann, T.; Guggenmos, A.; Goulielmakis, E. Multi-petahertz electronic metrology. *Nature* **2016**, *538*, 359363.
17. Hammond, T. J.; Monchoc, S.; Zhang, C.; Vampa, G.; Klug, D.; Naumov, A. Y.; Villeneuve, D. M.; Corkum, P. B. Integrating solids and gases for attosecond pulse generation. *Nature Photonics* **2017**, *11*, 594599.
18. Tancogne-Dejean, N.; Mcke, O. D.; Krtner, F. X.; Rubio, A. Ellipticity dependence of high-harmonic generation in solids originating from coupled intraband and interband dynamics. *Nature Communications* **2017**, *8*, 745.
19. Langer, F.; Hohenleutner, M.; Huttner, U.; Koch, S. W.; Kira, M.; Huber, R. Symmetry-controlled temporal structure of high-harmonic carrier fields from a bulk crystal. *Nature Photonics* **2017**, *11*, 227231.
20. Sivilis, M.; Taucer, M.; Vampa, G.; Johnston, K.; Staudte, A.; Naumov, A. Y.; Villeneuve, D. M.; Ropers, C.; Corkum, P. B. Tailored semiconductors for high-harmonic optoelectronics. *Science* **2017**, *357*, 303306.
21. Han, S.; Kim, H.; Kim, Y. W.; Kim, Y.-J.; Kim, S.; Park, I.-Y.; Kim, S.-W. High-harmonic generation by field enhanced femtosecond pulses in metal-sapphire nanostructure. *Nature Communications* **2016**, *7*, 13105.
22. Tancogne-Dejean, N.; Rubio, A. Atomic-like high-harmonic generation from two-dimensional materials. *Science Advances* **2018**, *4*, eaao5207.
23. Liu, H.; Li, Y.; You, Y. S.; Ghimire, S.; Heinz, T. F.; Reis, D. A. High-harmonic generation from an atomically thin semiconductor. *Nature Physics* **2016**, *13*, 262265.
24. Mikhailov, S. A. Non-linear electromagnetic response of graphene. *Europhysics Letters (EPL)* **2007**, *79*, 27002.

25. Bowlan, P.; Martinez-Moreno, E.; Reimann, K.; Elsaesser, T.; Woerner, M. Ultrafast terahertz response of multilayer graphene in the nonperturbative regime. *Physical Review B* **2014**, *89*, 041408(R).
26. Al-Naib, I.; Sipe, J. E.; Dignam, M. M. High harmonic generation in undoped graphene: Interplay of inter- and intraband dynamics. *Physical Review B* **2014**, *90*, 245423.
27. Al-Naib, I.; Sipe, J. E.; Dignam, M. M. Nonperturbative model of harmonic generation in undoped graphene in the terahertz regime. *New Journal of Physics* **2015**, *17*, 113018.
28. Cox, J. D.; Marini, A.; de Abajo, F. J. G. Plasmon-assisted high-harmonic generation in graphene. *Nature Communications* **2017**, *8*, 14380.
29. Yoshikawa, N.; Tamaya, T.; Tanaka, K. High-harmonic generation in graphene enhanced by elliptically polarized light excitation. *Science* **2017**, *356*, 736738.
30. Taucer, M.; Hammond, T. J.; Corkum, P. B.; Vampa, G.; Couture, C.; Thir, N.; Schmidt, B. E.; Lgar, F.; Selvi, H.; Unsuree, N. *et al.* Nonperturbative harmonic generation in graphene from intense midinfrared pulsed light. *Physical Review B* **2017**, *96*, 195420.
31. Baudisch, M.; Marini, A.; Cox, J. D.; Zhu, T.; Silva, F.; Teichmann, S.; Massicotte, M.; Koppens, F.; Levitov, L. S.; Garca de Abajo, F. J. *et al.* Ultrafast nonlinear optical response of Dirac fermions in graphene. *Nature Communications* **2018**, *9*, 1018.
32. Runge, E.; Gross, E. K. U. Density-Functional Theory for Time-Dependent Systems. *Physical Review Letters* **1984**, *52*, 997–1000.
33. van Leeuwen, R. Causality and Symmetry in Time-Dependent Density-Functional Theory. *Physical Review Letters* **1998**, *80*, 12801283.
34. Castro, A.; Marques, M.; Alonso, J. A.; Rubio, A. Optical properties of nanostructures

- from time-dependent density functional theory. *J. Comp. Theoret. Nanoscience* **2004**, *1*, 231–255.
35. Cahangirov, S.; Topsakal, M.; Aktürk, E.; Şahin, H.; Ciraci, S. Two- and One-Dimensional Honeycomb Structures of Silicon and Germanium. *Physical Review Letters* **2009**, *102*, 236804.
36. Qin, R.; Wang, C.-H.; Zhu, W.; Zhang, Y. First-principles calculations of mechanical and electronic properties of silicene under strain. *AIP Advances* **2012**, *2*, 022159.
37. Qin, R.; Zhu, W.; Zhang, Y.; Deng, X. Uniaxial strain-induced mechanical and electronic property modulation of silicene. *Nanoscale Research Letters* **2014**, *9*, 521.
38. Vampa, G.; Brabec, T. Merge of high harmonic generation from gases and solids and its implications for attosecond science. *Journal of Physics B* **2017**, *50*, 083001.
39. Andrade, X.; Strubbe, D. A.; Giovannini, U. D.; Larsen, A. H.; Oliveira, M. J. T.; Alberdi-Rodriguez, J.; Varas, A.; Theophilou, I.; Helbig, N.; Verstraete, M. *et al.* Real-space grids and the Octopus code as tools for the development of new simulation approaches for electronic systems. *Physical Chemistry Chemical Physics* **2015**, *17*, 31371–31396.
40. Castro, A.; Appel, H.; Oliveira, M.; Rozzi, C.; Andrade, X.; Lorenzen, F.; Marques, M.; Gross, E.; Rubio, A. octopus: a tool for the application of time-dependent density functional theory. *Phys. Stat. Sol. B* **2006**, *243*, 2465–2488.
41. Andrade, X.; Alberdi-Rodriguez, J.; Strubbe, D. A.; Oliveira, M. J. T.; Nogueira, F.; Castro, A.; Muguerza, J.; Arruabarrena, A.; Louie, S. G.; Aspuru-Guzik, A. *et al.* Time-dependent density-functional theory in massively parallel computer architectures: the octopus project. *J. Phys.: Cond. Matt.* **2012**, *24*, 233202.

42. Marques, M. A. L.; Oliveira, M. J. T.; Burnus, T. Libxc: a library of exchange and correlation functionals for density functional theory. *Comput. Phys. Commun.* **2012**, *183*, 2272–2281.
43. Castro, A.; Marques, M.; Rubio, A. Propagators for the time-dependent Kohn-Sham equations. *J. Chem. Phys.* **2004**, *121*, 3425–3433.

## Acknowledgement

We acknowledge financial support from the National Natural Science Foundation of China (NSFC) (11705185) and the Presidential Fund of China Academy of Engineering Physics (CAEP) (YZJLX2017002).